Three-dimensional mathematical modeling of local scour

Hao ZHANG*, Hajime NAKAGAWA**, Taisuke ISHIGAKI***, Yasunori MUTO**** and Yasuyuki BABA****

* Member, Doctoral Student, Kyoto Univ. (Yoshida-Honmachi, Sakyo-ku, Kyoto 606-8501)
** Member, Dr. of Eng., Professor, Kyoto Univ. (Shimomisu, Yoko-oji, Fushimi-ku, Kyoto 612-8235)
***Member, Dr. of Eng., Professor, Kansai Univ. (3-3-35 Yamate-cho, Suita-shi, Osaka 564-8680)
**** Member, Dr. of Eng., Kyoto Univ. (Shimomisu, Yoko-oji, Fushimi-ku, Kyoto 612-8235)

This study gives a description and some applications of a three-dimensional mathematical model, through which the local scour holes around hydraulic structures can be simulated. This model calculates the flow field by solving the Reynolds-averaged Navier-Stokes equations with the widely-used k-ε model for the turbulence closure. The local scour holes are assumed to take place in the form of bed load transport and modeled with a modified Ashida-Michiue formula. A finite volume method based on a moving unstructured mesh is employed in the formulation, which is able to resolve the flow and sediment transport in complex geometries with changeable boundaries. This is of significant meaning for engineering practices. The model is applied to predict two laboratory experiments. It is shown that the local sour profiles, together with the flow characteristics, have been reasonably reproduced.

Key Words: local scour, k-ε model, moving unstructured mesh, FVM

1. Introduction

Investigation of the local scour around hydraulic structures is of significant meaning in engineering practices. An excessive scour hole has a potential to undermine the foundation, which may lead to failures and disasters in a river training project. On the other hand, the wide spectrum of turbulences and sediment related problems induced by the local scour strongly correlate with the environmentally oriented communities, which is a great consideration in the campaign of the river restoration. There are many varieties of local scour systems due to different geometries and flow patterns. But in essence, local scour phenomenon is caused by the imbalance in sediment transport due to the local obstruction.

Most of the previous researches on the local scour around hydraulic structures are concerned with prediction of the equilibrium or design scour depth [1), 2)]. For example, Melville (1997) summarized many of the results from an extensive program of bridge scour research undertaken at the University of Auckland, New Zealand. An integrated approach for determination of design scour hole depth at bridge foundations was then proposed in terms of empirical enveloping curves accounting for the pertinent variables such as flow depth and intensity, sediment characteristics, approach channel geometry, foundation type, shape, size and alignment [3)]. Temporal variation of the local scour holes rapidly received an attention in the past decade. A brief summary has been made by Coleman et al. (2003) [4)]. Very recently, Dey and Barbhuiya (2005) constructed a semi-empirical model to calculate the change of the scour depth with time based on the concept of sediment conservativeness, considering the primary vortex system as the main agent of scour and assuming a layer-by-layer scouring process [5)]. These efforts are very important and necessary but far from enough because they involve strong empiricism and introduce many uncertainties. Moreover, the unknown of the geometry of the scour holes and information on the interaction between the flow and sediment transport is also a limitation. A further insight into the local scour around hydraulic structures requires more advanced models in 2D or 3D. Since the local flow in the vicinity of the scour holes exhibits obvious 3D characteristics, a 2D model is not attractive if the details need to be resolved. Instead, a 3D model is promising and becomes more and more popular nowadays. A brief summary of some recent studies on 3D modeling of local scour is given here.

Ushijima et al. (1992) proposed a method to estimate the local scour due to the cooling water jets discharged from power

stations [6]. The calculation of the local scour in forms of both bed load and suspended load was performed unsteadily in parallel with the calculation of the flow which was solved through the k-ε turbulence model. Ushijima (1996) later extended the model on the basis of Lagrangian-Eulerian formulation and found a great improvement compared with the previous one [7].

Omitting the transient term, Olsen and Melaaen (1993) calculated the scour hole around a cylinder by solving the 3D RANS (Reynolds-averaged Navier-Stokes) equation on a structured non-orthogonal grid with the k-ε model for the Reynolds stresses and the convection-diffusion equation for the sediment transport [8]. During the iteration process, the flow field and bed geometry at the previous iteration are used to calculate the new velocity and bed change. This procedure repeated until the maximum scour hole depth was equal to that observed in the experimental measurement. The model was later extended with transient terms by Olsen and Kjellesvig (1998) [9]. Bhuiyan et al. (2004) reported that the model was also able to simulate the flow and bed evolution around submerged and unsubmerged spurs [10]. As the structured mesh method was difficult to resolve complex geometries and moving boundaries, Olsen (2003, 2004) [11), 12)] further extended the model to an unstructured mesh system and it has been employed to simulate the formation of the meandering pattern in an initially straight alluvial channel [11].

Fukuoka et al. (1994) developed a 3D flow model with an empirical eddy viscosity equation and under the assumption of hydrostatic pressure [13]. The bed deformation model included the effect of non-equilibrium sediment transport processes. The simulation result for a bridge pier was in good agreement with the experimental result. The model was later improved and extended. According to the computation work carried out by Watanabe et al. (2001), it was also able to predict the flow and bed deformation around groins in a curved channel [14].

Peng et al. (1998) assumed that the flow field within each time step of the bed deformation was steady. A model was developed to simulate the equilibrium scour pattern around a spur dike, which integrated a modified k-ε turbulence model with a modified Meyer-Peter and Muller formula for sediment transport [15]. The model result was reported to be encouraging.

Yen et al. (2001) employed an LES (Large eddy simulation) approach with Smagorinsky's sub-grid scale turbulence model to calculate the flow field around a bridge pier [16]. The scour model solved the sediment continuity equation in conjunction with van Rijn's bed load transport formula [17]. Without re-computing the 3D flow field as the bed deformed, the shear stress obtained from the 3D flow field under flatbed conditions was modified according to the bed change. This has greatly reduced the computational time.

Nagata et al. (2002) reported a model based on a moving boundary-fitted coordinate system [18]. The velocity field and shear stress are calculated from a non-linear k-ε turbulence model. The bed deformation around a cylindrical pier was simulated by coupling the momentum equation of sediment with stochastic models for sediment pick-up and deposition. It was found that the proposed numerical model was able to reproduce the flow and scour geometry in the laboratory experiment with a sufficient accuracy.

According to the previous researches, it is found that the bottleneck of the state-of-the-art of the local scour simulation lies in the accurate modeling of the sediment behavior and the interaction between the flow and bed variation.

In this paper, the flow field is obtained by solving the unsteady RANS with the k-ε model for the turbulence closure. The wall function approach is applied in the near wall area. A modified Ashida-Michiue formula [19] is employed to evaluate the sediment transport rate. The bed variation (including the local scour) is accounted for with the sediment continuity equation. A moving unstructured mesh based FVM (Finite volume method) is adopted, and arbitrary polyhedral mesh up to six faces may be used in the calculation. Model verification is carried out by comparing the computed results with previous laboratory experiments.

2. Flow model

In a k-ε model, the RANS equations are used for the mean flow quantities only, while the time-averaged statistical turbulent fluctuations are modeled from the information of the mean flow by introducing a concept of eddy viscosity and constructing two transport equations for the turbulence kinetic energy k and its dissipation rate ε. A detailed explanation was given by Rodi (1980) [20].

The governing PDEs (Partial differential equations) in the k-ε model are integrated over a number of polyhedral CVs (Control volumes) covering the whole study domain in an FVM procedure. As the inner CV faces will cancel out, the summation of the integral equations for all the CVs leads to the global conservation equation. This is an inherent property of FVM and one of the most attractive advantages to use this method in engineering practices. The final conservation equations considering the mesh movement with the FVM formulation have the general form as follows.

$$\frac{\partial}{\partial t}\int_V dV + \int_S (\boldsymbol{u} - \boldsymbol{u}_m)\cdot \boldsymbol{n} dS = 0 \qquad (1)$$

$$\frac{\partial}{\partial t}\int_V \phi dV + \int_S \phi(\boldsymbol{u} - \boldsymbol{u}_m)\cdot \boldsymbol{n} dS = \int_S \Gamma \nabla\phi \cdot \boldsymbol{n} dS + \int_V b dV \qquad (2)$$

where t= the time; V= the volume of the CV; S= the CV face with a unit normal vector $\boldsymbol{n}$ directing outwards; ϕ = general conserved quantity representing either scalars or vector and tensor field components; $\boldsymbol{u}$= the fluid velocity vector whose Cartesian components are u_i or (u, v, w); $\boldsymbol{u}_m$= the velocity vector of CV face movement whose Cartesian components are u_{mi} or

(u_m, v_m, w_m); Γ = diffusion coefficient and b= the volumetric source of the quantity ϕ . Eq. (1) expresses the mass conservation and Eq. (2) stands for the conservation of other quantities such as the momentum. It is noted that on the left side of Eq. (2) there are transient terms and convective terms which are balanced by diffusive terms and source terms on the right. The equation system is mesh-independent and is valid for arbitrary polyhedral CVs. As a result, an FVM procedure is able to take full advantages of an unstructured mesh.

In this study, a collocated mesh is adopted and all the unknowns are defined at the center of the CV. Using the second order midpoint rule, Eq. (2) can be discretized in space term by term as follows.

$$\frac{\partial}{\partial t}\int_V \phi dV + \sum_f \phi_f \left[\left(\boldsymbol{u} - \boldsymbol{u}_m \right)_{f\perp} \boldsymbol{S}_f \right] = \sum_f \Gamma_f \left. \frac{\partial \phi}{\partial \boldsymbol{n}} \right|_f \boldsymbol{S}_f + b_P - s_P \phi_P \quad (3)$$

where subscript P= the present CV ; subscript f= the face of the CV; subscript $\perp$= the component of the quantity normal to the surface; $\boldsymbol{S}_f$ =the surface area vector; b_P= part of the source term containing all the contributions excluding unknown variables and $-s_P\phi_P$ = part of the source term including the unknown variables which can be treated implicitly. After the spatial discretization, the second order implicit Crank-Nicolson scheme is employed for the temporal integral. Eq. (1) is not directly solved, but is included in the SIMPLE (Semi-implicit method for pressure-linked equations) procedure to give the pressure correction. The final pressure correction equation is found to have the similar form as that of Eq. (2) and may be discretized in the same way. The readers interested in the detailed discretization methods are referred to Nakagawa et al. (2004) [21].

Since the mesh movement has been included in the governing equations, the solution of the equation system is related to the CV itself rather than the absolute location of the CV center in the Cartesian coordinate. As a result, it is no need to redistribute the solution from the current time step to the next time step even if a new mesh system is generated due to the change of domain geometries. On the other hand, the mesh movement may introduce artificial mass sources in the discretized equations, and this has a potential to accumulate and spoil the simulation. Therefore, the conservation of the space should also be satisfied when the CV changes its shape and/or position with time. That is, the summation of the volume fluxes through CV faces due to the mesh movement must equal the rate of the volume change. A mathematic interpretation is

$$\frac{\partial}{\partial t}\int_V dV - \int_S \boldsymbol{u}_m \cdot \boldsymbol{n} dS = 0 \quad (4)$$

If Eq. (4) is substituted into Eq. (1), one may find that Eq. (1) has a simpler form as

$$\int_S \boldsymbol{u} \cdot \boldsymbol{n} dS = 0 \quad (5)$$

From the viewpoint of computational conveniences, the mesh system is allowed to move only in the vertical direction for the time being. This makes it possible to use some simple approach to evaluate the volume fluxes and that the space conservation law Eq. (4) is automatically guaranteed at the same time. In this paper, the velocity of the movement of a CV face is determined from the difference in the mesh locations at two consecutive time steps (see Fig. 1 for the movement of a prismatic mesh), i.e.

$$\boldsymbol{u}_m = \frac{\boldsymbol{r}_c^{m+1} - \boldsymbol{r}_c^{m}}{\Delta t} \quad (6)$$

where $\boldsymbol{r}_c$ = center of the CV face, Δt= time step and superscript m, m+1= current time step and next time step, respectively.

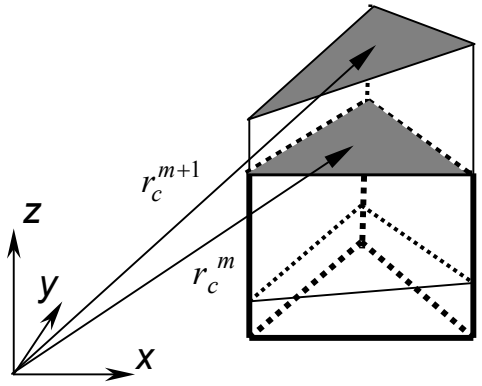

Fig. 1 Movement of a CV face at two consecutive time steps

The final algebraic equation system resulted from the discretization process may be written as

$$a_P \phi_P = \sum_{nb} a_{nb} \phi_{nb} + b_P \quad (7)$$

in which a is a coefficient for the unknown at the center of the approximated CV and the subscript nb stands for the neighboring CV. The coefficient matrix is generally sparse and non-symmetrical. Iterative methods based on Krylov subspaces are preferred. A preconditioned GMRES (Generalized minimal residual method) solver incorporated with an ILUTP (Incomplete LU factorization with threshold and pivoting) preconditioner given by Saad (2003) is employed here [22]. Before submitted to the solver, the relaxation method proposed by Patankar (1980) is implemented to increase the diagonal dominance of the coefficient matrix [23].

3. Scour simulation

In the absence of suspended load, the bed variation is due to the movement of bed load transport in a thin layer near the riverbed. The sediment continuity equation in the bed load layer is expressed by

$$\left(1-\lambda\right)\frac{\partial z_b}{\partial t} + \left[\frac{\partial q_{bx}}{\partial x} + \frac{\partial q_{by}}{\partial y} \right] = 0 \quad (8)$$

where z_b= riverbed elevation; λ = porosity of sediment on the riverbed; q_{bx} , q_{by} = bed load transport rate in x and y direction, respectively.

The total bed load transport rate is evaluated with the Ashida-Michiue formula as below [19]

$$\frac{q_b}{\sqrt{(s-1)gd^3}} = 17\tau_{*e}^{3/2}\left(1-\sqrt{\frac{\tau_{*c}}{\tau_*}}\right)\left(1-\frac{\tau_{*c}}{\tau_*}\right) \tag{9}$$

where q_b= bed load discharge per unit width; s= specific gravity of sediment; g= gravitational acceleration; d= diameter of sediment; $\tau_{*e}, \tau_{*c}, \tau_*$ = dimensionless effective shear stress, critical shear stress and shear stress, respectively. The dimensionless shear stress is connected with the squared friction velocity u_*^2 and is defined as

$$\tau_* = \frac{u_*^2}{(s-1)gd} \tag{10}$$

In the simulation of the local scour, the bed slope effect on the sediment transport is not negligible. It appears that the bed slope will affect the bed load transport in three ways: (a) the threshold condition, i.e. the condition just sufficient to initiate sediment motion; (b) the effective shear stress acting on the particle and (c) the direction of the sediment movement.

The investigation of the bed slope effect received a great attention and achieved significant development in the past century. Many researchers divided the riverbeds into longitudinal beds and transverse beds and developed a vast number of formulae. A brief view was given by Dey (2003) [24]. However this kind of treatment seems not very suitable for the 3D modeling of local scouring around structures according to the authors' numerical experiments [25]. This is due to the fact that the geometry of the scour holes is highly three-dimensional and that the magnitude of the velocity components in the local scour area is generally comparable. In view of these arguments, a 3D analysis of the bed slope effect is presented hereafter.

The forces acting on a sediment particle placed on a bed under the threshold condition are shown in Fig. 2 (where $\boldsymbol{n}$ is the normal direction of the bed plane and α , β and γ are direction angles). These forces are simplified as the submerged particle weight $\boldsymbol{W}$ and the hydrodynamic force $\boldsymbol{F}$. In a Cartesian coordinate system, the vectors in Fig. 2 may be written as

$$\boldsymbol{n} = \cos\alpha\boldsymbol{i} + \cos\beta\boldsymbol{j} + \cos\gamma\boldsymbol{k} \tag{11}$$

$$\boldsymbol{W} = W\cdot\boldsymbol{k} \tag{12}$$

$$\boldsymbol{F} = F\left(f_x\boldsymbol{i} + f_y\boldsymbol{j} + f_z\boldsymbol{k}\right) \tag{13}$$

where $\boldsymbol{i}$, $\boldsymbol{j}$ and $\boldsymbol{k}$ = the unit vectors in x, y and z direction, respectively; f_x, f_y and f_z = the direction cosines of the fluid force $\boldsymbol{F}$ which can be directly obtained from the turbulence model.

In the analysis of sediment transport, the hydrodynamic force is usually divided into a lift force and a drag force. For reasons of simplicity, the ratio of the lift force to the submerged particle weight is assumed to be relatively small [17]. Hence the fluid force $\boldsymbol{F}$ is parallel to the solid wall. Consequently, the resulted driving force is written as

$$\begin{aligned}\boldsymbol{F}_{\mathrm{R}} = &\left(W\cos\gamma\cos\alpha + f_xF\right)\boldsymbol{i} + \left(W\cos\gamma\cos\beta + f_yF\right)\boldsymbol{j} \\ &+\left(-W\sin^2\gamma + f_zF\right)\boldsymbol{k}\end{aligned} \tag{14}$$

And the magnitude of the corresponding stabilizing force is

$$F_S = -W\cos\gamma\tan\varphi \tag{15}$$

in which $\tan\varphi$ = the friction coefficient and φ = the angle of sediment repose underwater. It is noted that the direction of the stabilizing force is opposite to the resulted driving force as described in Eq. (14).

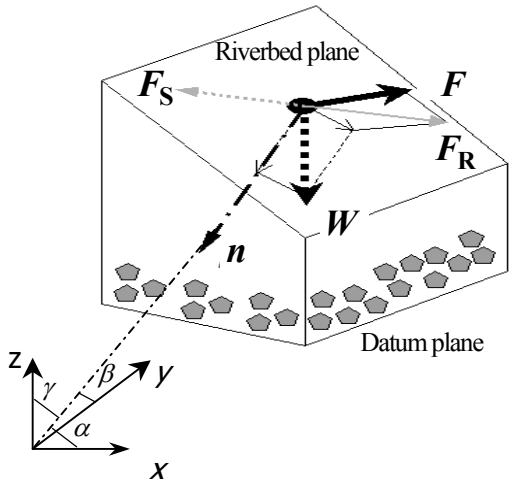

Fig. 2 Definition sketch of sediment threshold condition

At a relatively high Reynolds number, the fluid force will act through the center of the particle. Comparing the forces above with those on a horizontal bed, the difference can be expressed by a bed slope factor [17]. In terms of shear stress, the threshold condition reads

$$\tau_c = K\tau_{c0} \tag{16}$$

$$K = \frac{\sqrt{m^2 - \sin^2\gamma + \cos^2\gamma\tan^2\varphi} - m}{\tan\varphi} \tag{17}$$

$$m = f_x\cos\gamma\cos\alpha + f_y\cos\gamma\cos\beta - f_z\sin^2\gamma \tag{18}$$

where τ_c, τ_{c0} = the critical shear stress for a sloping bed and a horizontal bed, respectively. One may find that the bed slope factor K is a function of not only the bed slope and angle-of-repose but also the direction of the fluid force. Liu (1991) and Dey (2003) also theoretically derived a bed slope factor with the similar force analysis [24), 26]. However, their formulae are quite complex and seem very difficult to ensure a numerical implementation without simplifications.

The effect of the bed slope on the effective shear stress may

be observed in Eq. (14). One can find that a part of the sediment gravity contributes to the effective shear stress. This contribution should be taken into account in the Ashida-Michiue formula. As is known that the direction of the sediment movement does not coincide with the flow direction on a sloping bed. A reasonable treatment is to assume that the sediment movement follows the direction of the resulted driving force. Then the sediment transport direction is explicitly obtained from Eq. (14).

4. Solution procedure

The calculation sequences for the flow and bed evolution may be summarized as follows.

Starting from an initial riverbed geometry, all variables are assigned initial values at $t = t_0$. Time is advanced and calculation starts.

(1) Solve the momentum equations for each velocity component, in which the other velocity components, the pressure, the eddy viscosity, the turbulence kinetic energy and its dissipation rate are treated as known (initial values or values at the previous time step).

(2) The resulted velocity field is used to calculate the mass fluxes through CV faces. Solve the pressure correction equation and improve the velocity field.

(3) Solve the transport equations for the turbulence kinetic energy and its dissipation rate, respectively. Update the eddy viscosity.

(4) Repeat the above procedures until the residual level becomes sufficiently small or the prescribed maximum iteration step number is reached.

(5) Use the flow field and the Ashida-Michiue formula to evaluate the sediment transport rate.

(6) Solve the sediment continuity equation to get the bed variation and the bed geometry. Check the bed slopes and adjust the bed elevation until the angles of all the local beds are not greater than the angle of sediment repose [27].

(7) Generate a new mesh according to the bed geometry. Time is then forward.

(8) Check the maximum bed variation.

  (a) If the maximum bed change is larger than a prescribed value (e.g. 8% of the initial water depth is used in this paper), return to (1) and repeat the preceding calculation.

  (b) If the maximum bed change is relatively small, the flow field is assumed to be unchanged, only the sediment routine starting from step (5) is repeated.

  (c) If the maximum bed change is very small (for example, less than 10^{-4} cm/s), an equilibrium condition may be assumed.

(9) Stop the computation if the equilibrium condition is reached or a specified time is covered.

5. Application

The turbulence model and the proposed unstructured mesh method have been verified to be capable of predicting some selected flow phenomena under fixed bed conditions with reasonable accuracy [21]. In this paper, emphasis is put on the movable bed conditions.

5.1 Local scour due to a series of embayments

The local scouring around embayment is one of the most commonly encountered hydraulic phenomena. A series of experiments have been carried out by Muto et al. (2003) in a straight compound flume with a slope of 1/700 [28]. One of the non-submerged cases is selected in this verification. The hydraulic condition for the experiment is shown in Table 1.

Table 1 Hydraulic condition for the experiment

Discharge	Water Depth	Mean Velocity	Re. Number	Fr. Number
8.23 l/s	4.30 cm	28.57 cm/s	12,285	0.44

Ten successive embayments are formed by equipping 9 spur dykes in the flood plain area (see Fig. 3). The initial riverbed is covered by 10cm-thick artificial sands with a mean diameter of d=1.34mm. And the density of the sediment particles is 2.24g/cm^3. The riverbed is observed to reach an equilibrium state after a continuous running of 24 hours.

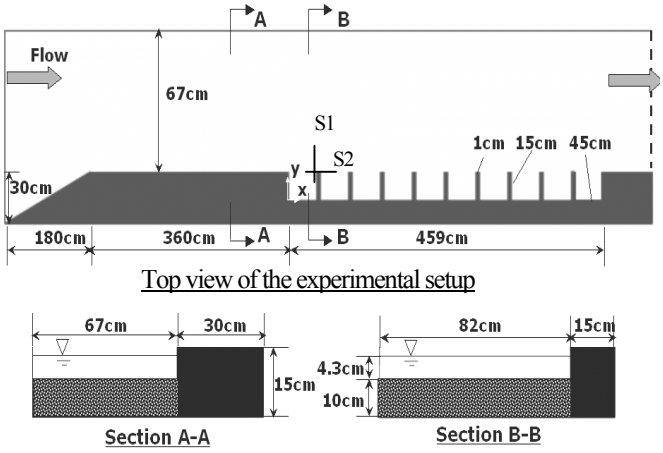

Fig. 3 Experimental setup for a series of embayments

The computational domain does not cover the whole domain of the experiment. The input boundary begins 10*b* (here *b* is the length of the spur dyke, i.e. 15cm) upstream from the first embayment. The longitudinal velocity along the vertical direction is assumed to satisfy the logarithmic profile at the inlet. The outlet flow boundary is 20*b* downstream from the last embayment. A total number of 14,196 hexahedral mesh (all the mesh surfaces are quadrilaterals) is generated for the

computation. A steady-state calculation is carried out on the flat bed at the beginning. The resulted velocity field serves as the initial condition for the movable bed computation. The mesh system changes its location according to the bed variation, but the total number of the mesh is unchanged.

The final bed variation around the first two embayments and the last two embayments at the equilibrium condition is depicted in Fig. 4 and Fig. 5, respectively.

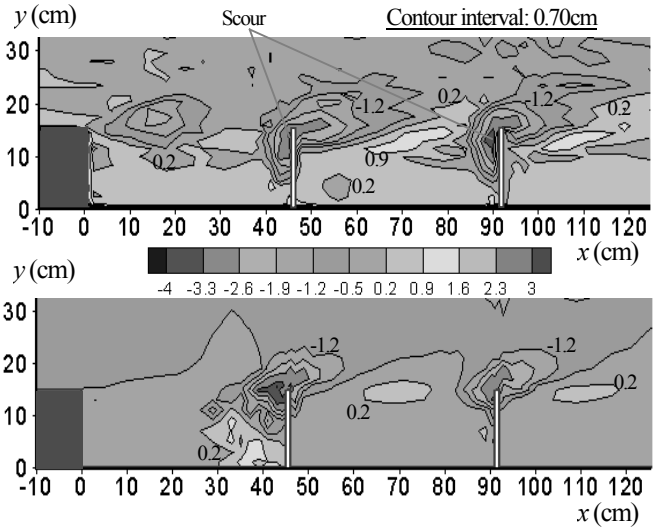

Fig. 4 Bed variation around the first two embayments (Experiment: Top; Computation: Bottom)

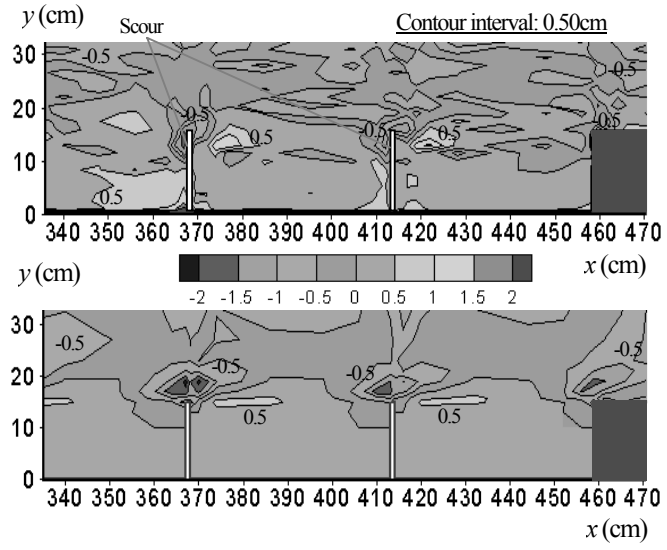

Fig. 5 Bed variation around the last two embayments (Experiment: Top; Computation: Bottom)

The result is encouraging. Local scour holes occur at the toes of all the spur dykes. This can be found in both experimental measurements and computational results (Fig.4 and Fig.5). Moreover, the geometries of the scour holes are generally similar. The deepest scour holes take place in the vicinities of the first and the second spur dykes. According to the measurement data, the values are 3.69cm and 4.37cm, respectively. In the computation, these values are predicted as 4.03cm and 3.68cm, respectively. There is a smaller scour a little downstream from the front of the first embayment in the experiment. This may be due to the sudden widening of the channel. But this phenomenon is not resolved in the computation. It indicates that the shear stress has been under-estimated in the junction zone (i.e. the area between the main channel and the embayment). On the other hand, a large area of deposition has been predicted along the bank in the corner area of the first embayment, which is not observed in the experiment. It demonstrates an over-estimation of the shear stress. The limitation of the k-ε model and the relatively coarse mesh may be responsible for these differences. Some performances of the k-ε model and a non-linear k-ε model for fixed bed flow predictions can be found in Nakagawa et al. [21].

From the third to the final spur dyke, the maximum depth of the scour hole is much smaller compared with the first two, which may be easily observed in Fig. 5. This also provides a possible way to save money for the toe protection in engineering practices.

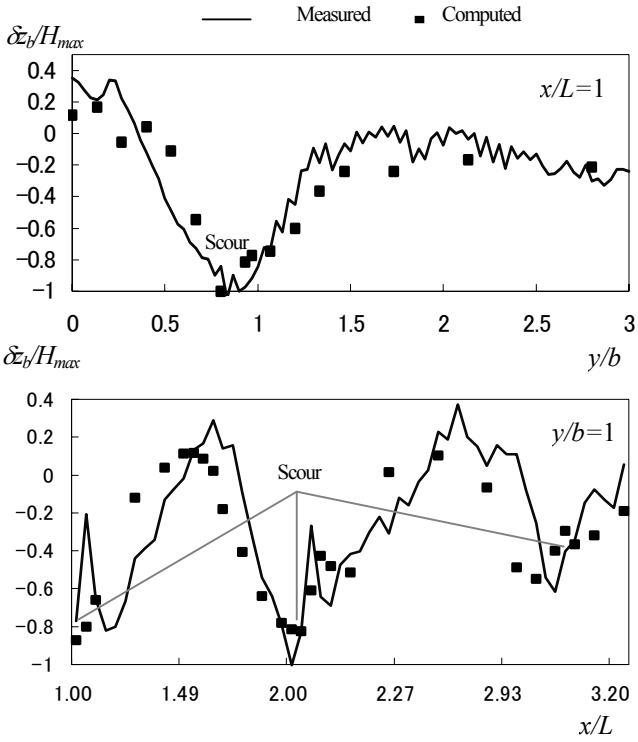

Fig. 6 Local scour hole profiles (Transverse section S1: Top; Longitudinal section S2: Bottom)

A more quantitative comparison is carried out for the local scour hole profiles along two representative cross-sections (see Fig. 6). The location of the two sections is illustrated in Fig. 3. They are transverse and longitudinal sections near the head of the first spur dyke (Section S1 is defined by $x/L=1$, in which L is the length of the embayment, and Section S2 is defined by $y/b=1$). The value of the bed deformation δz_b has been

normalized by the maximum scour depth H_{max} at the corresponding section. One may find that the numerical result is in good agreement with that of the experimental data.

Finally, the comparison of the velocity vectors (*u, v*) at *z*=2.3cm from the datum level is shown in Fig. 7. The experimental data is obtained with electromagnetic velocity meters after the final bed was fixed with cements (100 samples at a frequency of 10Hz for each point). Only the first three embayments are shown due to the fact that the flow around the remaining embayments is quite similar to the third one.

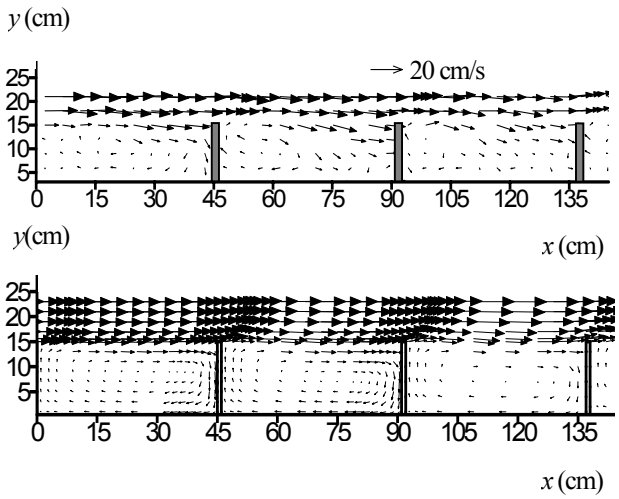

Fig. 7 Velocity vectors (*u, v*) at z=2.3cm
(Experiment: Top; Computation: Bottom)

The details of the flow field have been reasonably captured although the mesh adopted here is relatively coarse. For instance, the large eddy in each embayment is evidently observed. Nevertheless, the magnitude of the velocity in the junction zone seems to be under-estimated. This may also give an explanation why the predicted bed variation in the junction zone (Fig. 4 and Fig. 5) is simpler than that plotted from the experimental data.

5.2 Local scour around a submerged spur dyke

Hydraulic structures such as spur dykes usually suffer from overtopping flow during the flood season, which is of great interests in engineering practices. Ishigaki and Baba (2004) investigated the local scour induced by the flow around both non-submerged and submerged spur dykes experimentally [29]. Two kinds of spur dyke were tested in the experiments: an attracting type and a deflecting type. The spur dyke model was set on one side of the channel. The channel was 10m long, 1.0m wide and 0.3m deep, which was equipped with a discharge control system. A 1.8m long movable bed was located in the middle part of the channel. It was filled with 0.2m-thick sand with the mean diameter of 0.26mm. The experiment setup and hydraulic conditions for one of the submerged deflecting spur dyke are shown in Fig. 8 and Table 2, respectively. The shape and the size of the spur dyke are also depicted in Fig. 8.

Table 2 Hydraulic condition for the experiment

Discharge	Water Depth	Mean Velocity	Re. Number	Fr. Number
21.12 l/s	10.56 cm	20.0 cm/s	21,120	0.20

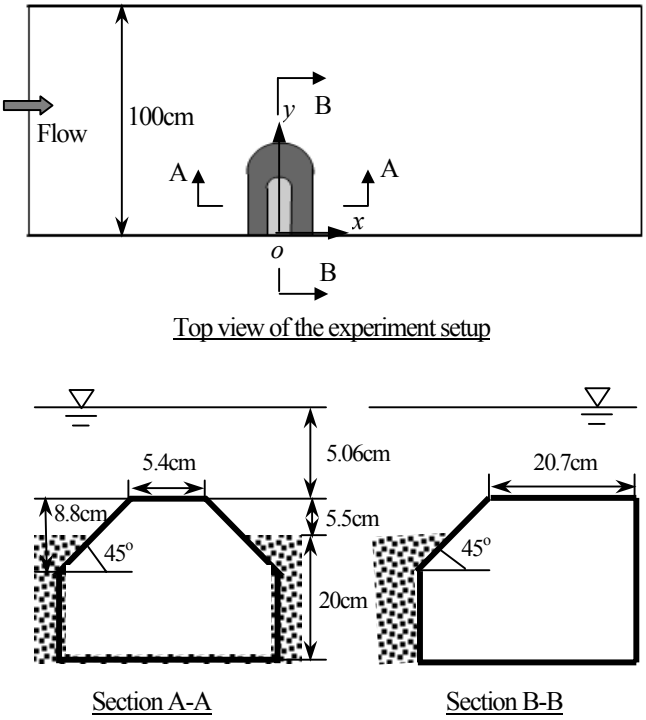

Fig. 8 Experimental setup for the submerged spur dyke

The overtopping ratio (water depth to the spur dyke height) in this verification case is 1.92. Measurements were carried out after one hour from the beginning of the experiment, which include the bed variation, the velocity components (longitudinal and vertical) and the water surface variation. The measurement devices include a laser level meter, an electromagnetic velocitmeter and an ultra-sonic level meter.

This simulation involves strongly 3D turbulent flow, complex but important hydraulic structure and movable irregular riverbed. Moreover, all those aspects are interacted with each other. The predominant structured mesh methods are not suitable in this case. As a result, successful calculation of this kind of problem has been rarely completed to the authors' knowledge.

In order to diminish the boundary effect, the inlet boundary and the outlet boundary are selected far enough from the spur dyke in the computation. A total number of 28,944 polyhedral mesh is used. The unstructured mesh consists of both hexahedra and prisms. With this kind of meshing strategy, the study domain can be accurately resolved. The mesh around the spur dyke is shown in Fig. 9.

In the computation, a logarithmic velocity profile in the vertical direction is assumed at the inlet boundary. The turbulent quantities k and ε are specified corresponding to a viscosity ratio of 10.0 and taking the turbulence intensity 8%.

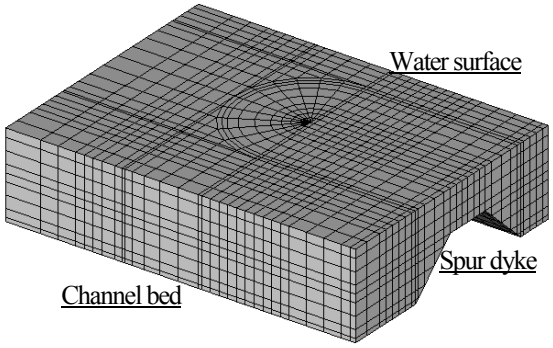

A bird's view of the 3D mesh over the flume

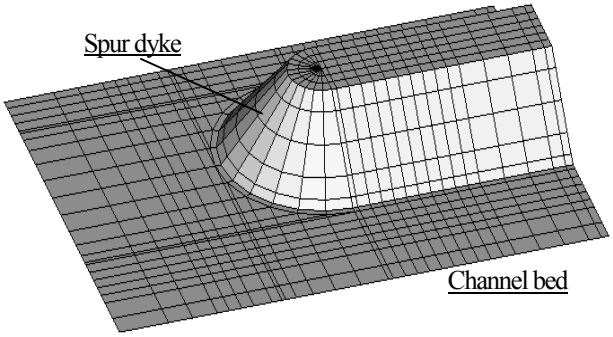

Mesh on the surface of the bed and the spur dyke

Fig. 9 Initial mesh system around the spur dyke (not to scale)

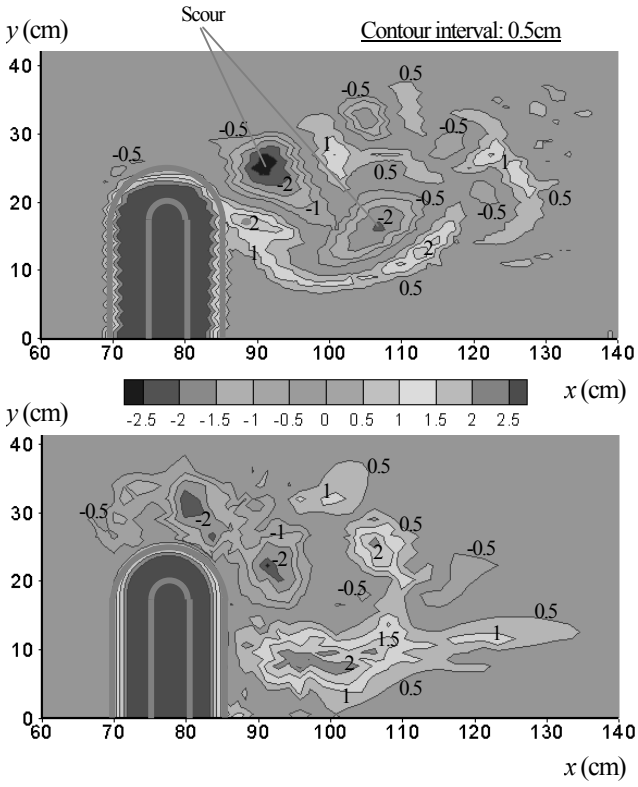

Fig. 10 Bed variation around the spur dyke after 1 hour (Experiment: Top; Computation: Bottom)

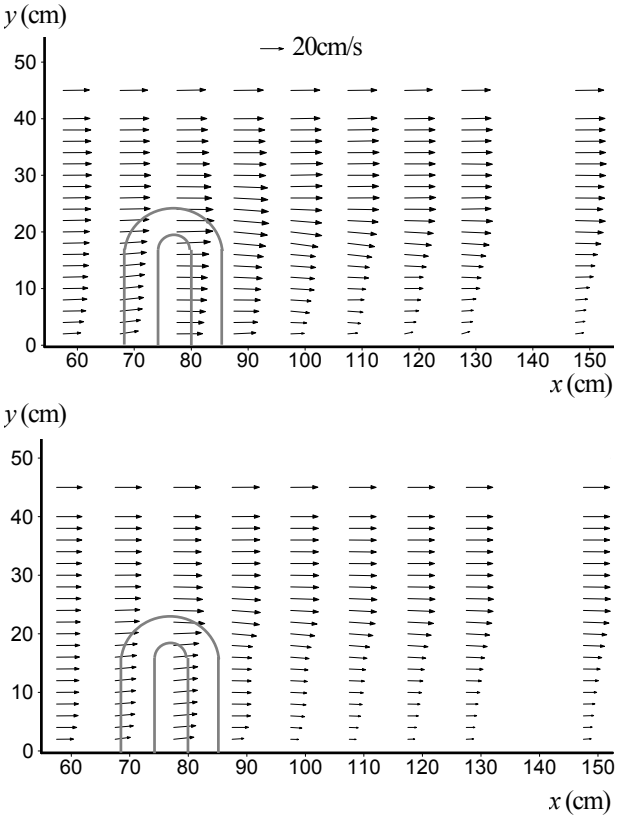

Fig.11 Velocity vectors (*u, w*) at *z*=6.5cm (i.e. 1cm over the spur dyke top) (Experiment: Top; Computation: Bottom)

Either the experiment or the computation shows that the significant bed deformation only occurs around the spur dyke area. Fig. 10 is the comparison of the bed variation near the spur dyke with the same scale.

In the experiment, there are two big scour holes as shown in Fig.10 (top). One is located near the downstream head of the spur dyke with a depth of 2.78cm. Another one is in the downstream side of the spur dyke, which has a depth of 2.05cm. The calculation also gives two obvious scour holes, the depths of which are 2.71cm and 2.33cm, respectively. The positions are depicted in Fig. 10 (bottom). It may be also observed that the predicted locations are a little more upstream than the measured ones. This may indicate that there are some differences in the distribution of the shear stress around the head of the spur dyke. The inherent defect of the k- ε model may be the main reason. Nevertheless, if the uncertainties involved in the movable bed experiment are taken into account, such conclusion may be drawn that the basic scour-deposition pattern has been reasonably reproduced in this simulation.

Another comparison is the velocity vectors (*u, w*) at *z*=6.5cm (i.e. 1cm over the top of the spur dyke). In the experiment, the velocity was measured with an L-shape electromagnetic velocimeter after the bed was fixed with cement powder (500 samples at a frequency of 10Hz for each point). It is noted that the computed velocity vectors have been interpolated to the points measured in the experiment (see Fig. 11). In the whole domain, the longitudinal velocity is predominant in this layer. Nevertheless there are some inflections in the proximity of the spur dyke if one takes a careful look at the experimental result

(Fig. 11, top). The flow over the spur dyke is accelerated near the head. There is a downward flow after the flow passes the top of the spur dyke. The same phenomenon has been predicted by the calculation (Fig. 11, bottom). But the predicted longitudinal velocity is a bit smaller than the measurement. As the flow structure and the bed configuration are closely interacted with each other. It is very difficult to analyze quantitatively the accuracy of them separately. If one can have a compare with Fig. 10 and Fig. 11 at the same time, one may find more confidence in the prediction capability of the current model.

The computed velocity vectors (u, v) in a horizontal plane z=2.0cm is plotted in Fig. 12. Due to the shortage of data, the comparison with experimental result is not fulfilled in this paper.

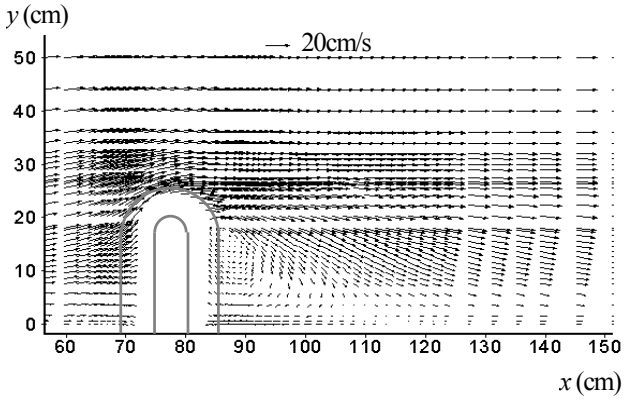

Fig. 12 Computed velocity field (u, v) at z=2.0cm

The flow velocity diverts at the head of the spur dyke. Behind the spur dyke, a horizontal vortex is evidently observed. At the center of the vortex, the flow is almost stagnant. These observations have also been found in the similar experiment research of submerged groins carried out by Kawaguchi et al. (2004) [30]. This also demonstrates that numerical model provides an effective way to understand the details of the local scour phenomena and some of which may be very difficult to resolve if not impossible with experimental methods.

6. Conclusions

A 3D mathematical model has been presented, which combines a k-ε turbulence model with a scour model and can be used for local scour prediction.

The sediment transport and the interaction between the flow and the bed morphology have been accentuated, and prediction of which has been considered to be one of the weakest points of most existing models to date. The local scour is assumed to take place in the form of bed load transport. The transport rate is evaluated based on the Ashida-Michiue formula. Extension has been made for a sloping bed from the perspective of 3D force analysis. This can take into account the local scour effect on the sediment movement. A moving unstructured mesh is adopted which may accurately resolve the boundary changes and include the corresponding information into the flow model.

The proposed model has been applied to two kinds of different flow phenomena in laboratory flumes including both non-submerged and submerged spur dykes. Comparison of the computed result with the experimental data demonstrates that the fundamental aspects of the flow and sediment behavior can be reasonably reproduced. Based on the unstructured mesh, the model may serve as a promising tool in the understanding of the local scouring around hydraulic structures in actual rivers.

Nevertheless, there are still some differences in the comparison of experiments and calculations. Despite of the uncertainties involved in the movable bed experiments, the numerical model itself has some space for improvements. In the turbulence module, the authors have tested both the standard k-ε model and a non-linear k-ε model under fixed bed conditions [21]. Although both kinds of models may lead to reasonable results in engineering practices, it was found that the non-linear k-ε model should be preferred whenever a more accurate simulation was required. However, the non-linear k-ε model sometimes failed to converge under movable bed conditions with the proposed moving unstructured mesh methods in this paper. This deserves further researches. Moreover, although the authors have tried to construct the scour model from the perspective of 3D space, the proposed model has included much empiricism from lower dimensions (1D and 2D). For example, the Ashida-Michiue formula, as well as many other bed load transport formulae, was originally concluded in 1D space from such flows that the longitudinal velocity was predominant. However, in the proximity of the scour holes, the flow showed obvious 3D characteristics. The magnitude of the three velocity components was generally comparable. As a result, the use of the conventional formulae might lead to questionable simulation. This should be paid much attention in a fully 3D model.

Acknowledgement

This study is financially supported by the Monbukagakusho (Ministry of Education, Culture, Sports, Science and Technology, Japan) under Grant No.14350265.

REFERENCES

1) Chang, H.H., Fluvial Processes in River Engineering, A Wiley-Interscience Publication, John Wiley & Sons, Inc., 1988
2) Kothyori, U.C. and Ranga Raju, K.G., Scour around spur dikes and bridge abutments, Journal of Hydraulic Research, IAHR, Vol.39, No.4, 2001, pp.367-374
3) Melville, B.W., Pier and abutment scour: integrated approach, Journal of Hydraulic Engineering, ASCE, Vol.123, No.2, 1997, pp.125-136

4) Coleman, S.E., Lauchlan, C.S. and Melville, B.W., Clear-water scour development at bridge abutments, Journal of Hydraulic Research, IAHR, Vol.41, No.5, 2003, pp.521-531
5) Dey, S. and Barbhuiya, A.D., Time variation of scour at abutments, Journal of Hydraulic Engineering, ASCE, Vol.131, No.1, 2005, pp.11-23
6) Ushijima, S., Shimizu, T., Sasaki, A. and Takizawa, Y., Prediction method for local scour by warmed cooling-water jets, Journal of Hydraulic Engineering, ASCE, Vol.118, No.8, 1992, pp.1164-1183
7) Ushijima, S., Arbitrary Lagrangian-Eulerian numerical prediction for local scour caused by turbulent flows, Journal of Computational Physics, Vol.125, 1996, pp.71-82
8) Olsen, N.R.B. and Melaaen, M.C., Three-dimensional calculation of scour around cylinders, Journal of Hydraulic Engineering, ASCE, Vol.119, No.9, 1993, pp.1048-1054
9) Olsen, N.R.B. and Kjellesvig, H.M., Three-dimensional numerical flow modeling for estimation of maximum local scour depth, Journal of Hydraulic Research, IAHR, Vol.36, No.4, 1998, pp.579-590
10) Bhuiyan, ABM F., Huque, F. and Saifuddin, AKM, Numerical modeling of flow pattern and bed evolution around spur-type structures, Proceedings of the 9th International Symposium on River Sedimentation, Oct. 18-21, 2004, Yichang, China, pp.1497-1502
11) Olsen, N.R.B., Three dimensional CFD modeling of self-forming meandering channel, Journal of Hydraulic Engineering, ASCE, Vol.129, No.5, 2003, pp.366-372
12) Olsen, N.R.B., A Three-dimensional Numerical Model for Simulation of Sediment Movements in Water Intakes with Multiblock Option: User's Manual, the Norwegian University of Science and Technology, 2004
13) Fukuoka, S., Tomita, K., Hotta, T. and Miyagawa, T., Practical numerical simulation of local scour around a bridge pier, Journal of Hydraulic, Coastal and Environmental Engineering, JSCE, No. 497(2-28), 1994, pp.71-79 (in Japanese)
14) Watanabe, A., Fukuoka, S., Yasutake, Y. and Kawaguchi, H., Groin arrangements made of natural willows for reduction bed formation in a curved channel, Advances in River Engineering, JSCE, Vol.7, 2001, pp.285-290 (in Japanese)
15) Peng, J., Tamai, N., Kawahara, Y. and Huang, G.W., Numerical modeling of local scour around spur dykes, Proceedings of 28th IAHR Congress, 1998 (CDs)
16) Yen, C.J., Lai, J.S. and Chang, W.Y., Modeling of 3D flow and scouring around circular piers, Proc. Nati. Sci. Counc. ROC (A), Vol.25, No.1, 2001, pp.17-26
17) van Rijn, L.C., Principles of Sediment Transport in Rivers, Estuaries and Coastal Seas, AQUA Publications, Amsterdam, The Netherlands, 1993
18) Nagata, N. Hosoda, T., Nakato, T. and Muramoto, Y., 3D numerical simulation of flow and local scour around a cylindrical pier, Journal of Hydroscience and Hydraulic Engineering, Vol.20, No.1, 2002, pp.113-125
19) Ashida, K. and Michiue, M.: Studies on bed load transportation for nonuniform sediment and river bed variation. Disaster Prevention Research Institute Annuals, Kyoto Univ., No.14B, 1971. (in Japanese)
20) Rodi, W., Turbulence Models and Their Application in Hydraulics - a State of the Art Review, University of Karlsruhe, Karlsruhe, Germany, 1980
21) Nakagawa, H., Zhang, H. Ishigaki, T. and Muto, Y., Prediction of 3D flow field with non-linear k-ε model based on unstructured mesh, Journal of Applied Mechanics, JSCE, Vol.7, 2004, pp.1077-1088
22) Saad, Y., Iterative Methods for Sparse Linear System (Second Edition), Society for Industrial & Applied Mathematics, 2003
23) Patankar, S.V., Numerical Heat Transfer and Fluid Flow, McGraw-Hill, New York, 1980
24) Dey, S., Threshold of sediment motion on combined transverse and longitudinal sloping beds, Journal of Hydraulic Research, IAHR, Vol.41, No.4, 2003, pp.405-415
25) Nagakawa, H., Zhang, H. and Muto, Y., Modeling of sediment transport in alluvial rivers with spur dykes, Proceedings of the 9th International Symposium on River Sedimentation, Oct. 18-21, 2004, Yichang, China, pp.1484-1491
26) Liu, B.Y., Study on Sediment Transport and Bed Evolution in Compound Channels, Ph. D Thesis, Kyoto University, 1991
27) Zhang, H., Nakagawa, H., Ishigaki, T. and Muto, Y., Prediction of 3D flow field and local scouring around spur dykes, Annual Journal of Hydraulic Engineering, JSCE, vol.49, 2005, pp.1003-1008
28) Muto, Y., Kitamura, K., Khaleduzzaman, A.T.M. and Nakagawa, H., Flow and bed topography around impermeable spur dykes, Advances in River Engineering, JSCE, Vol.9, 2003 (in Japanese)
29) Ishigaki, T. and Baba, Y., Local scour induced by 3D flow around attracting and deflecting groins, Proceedings of Second International Conference on Scour and Erosion, Meritus Mandarin, Singapore, Nov, 14-17, 2004, pp.301-308
30) Kawaguchi, H., Fukuoka, S. and Watanabe, A., Flow and hydrodynamic force distributions of submersed groins for different groin angles, Annual Journal of Hydraulic Engineering, JSCE, Vol.48, 2004, pp.137-142 (in Japanese)

(Received: April 15, 2005)